Proceedings of the 7th International Young Geotechnical Engineers Conference – Scott (Ed.)

The time dependent behavior of a trial embankment on Mexico City clay

Le comportement dépendant du temps d'un remblai d'essai sur l'argile de la ville de México

Renata A. González R., Miguel A. Mánica M. & Efraín Ovando Shelley
Geotechnics, Engineering Institute, UNAM, México, RGonzalezR@iingen.unam.mx

ABSTRACT: Given the extremely difficult subsoil conditions at the site of the now-abandoned project for the New International Airport for Mexico City, a series of test embankments were built to test different foundation solutions for the runways. In this paper, we look at the performance of the reference embankment, where no special foundation or soil improvement technique were adopted. Its behaviour is interpreted by means of a finite element simulation, in which an advanced elasto-visco-plastic constitutive model was implemented from available formulations in the literature. The implemented model incorporates key features of the behaviour of Mexico City Clay, such a time-dependency, long term deformations, and an anisotropic flow surface. Results provide an assessment of the constitutive description adopted.

RÉSUMÉ : Compte tenu des conditions extrêmement difficiles du sous-sol sur le site du projet, maintenant abandonné, du Nouvel Aéroport International de Mexico, une série de remblais d'essai ont été construits pour tester différentes solutions de fondation pour les pistes. Dans ce document, nous analysons les performances du remblai de référence, pour lequel aucune technique spéciale de fondation ou d'amélioration du sol n'a été adoptée. Son comportement est interprété au moyen d'une simulation à éléments finis, dans laquelle un modèle constitutif élasto-visco-plastique avancé a été mis en œuvre à partir de formulations disponibles dans la littérature. Le modèle implémenté intègre les principales caractéristiques du comportement de l'argile de Mexico, telles que la dépendance au temps, les déformations à long terme et une surface d'écoulement anisotrope. Les résultats fournissent une évaluation de la description constitutive adoptée.

KEYWORDS: embankment, time-dependency, anisotropy, soft clay, finite element simulation

1 INTRODUCTION.

In 2014, the plans to construct the New International Airport for Mexico City (NAICM, acronym in Spanish) were reactivated (SCT, 2014). The project would be built in the area of the former Texcoco Lake. The geotechnical design of the project represented a most demanding technical challenge, mainly due to the remarkable characteristics of the subsoil at the site. Test embankments were built to assist in the design of the runways. This paper addresses the performance of the reference embankment (RE), which is interpreted through finite element simulations. The embankment essentially applies a surface load on the subsoil without any treatment and, therefore, provides an excellent opportunity to assess, on a large scale, the performance of constitutive relationships for the characterisation of the time-dependent behaviour of Mexico City clay. The constitutive model employed is a variation of the elasto-viscoplastic model (EVP) of Yin and Graham (1999), in which the anisotropic yield function and evolution laws proposed by Wheeler et al. (2003) are included. The resulting model was implemented within a commercial FE code and employed in the simulation of the RE.

1.1 *Subsoil conditions at Texcoco*

The Texcoco Lake is located within the Mexico Basin, an endorheic basin closed during the Pleistocene-Holocene transition as a consequence of the intense volcanic activity forming the Chichinautzin Mountain Range (Mooser, 1956; Vázquez-Sánchez and Jaimes-Palomera, 1989), located south of Mexico City. The closure of the basing originated a system of interconnected lakes. This lake system has been progressively drained and a large portion of the city now rests on top of the former lake bed. The unique depositional environment, affected by periods of intense volcanic activity, resulted in very soft clayey and silty soils with an open and random structure (Mitchell, 1956) and exceptional index and mechanical properties (Ovando – Shelley, 2011). The former lake of Texcoco area is characterized by containing clay deposits that extend to depths greater than 50 m. These deposits exhibit extremely large void ratios and water contents, as well as notably high Atterberg limits. They also show very high compressibility and low undrained shear strength although friction angles may be rather large given the presence of ostracods and microscopic volcanic glass interspersed within the clay particles (Valderrama, 2013). The NAICM zone is also subjected to regional subsidence, caused by the extraction of water from the aquifers underlying the former lake bed (Ovando-Shelley et al., 2007, 2013). The water table is quite shallow, but hydrostatic conditions are only found up to depths between 10 and 23 m. At greater depths, pressure depletion occurs caused by the extraction of water from the deep aquifers.

2 REFERENCE EMBANKMENT

Different foundation solutions for the runways were considered. The test embankments were constructed in an area designated at the south portion of the premises to assess their performance.

Alternatives studied included: the reference embankment, a partial mass compensation system, piled embankment, rigid inclusions, preloading with sand drains, preloading with prefabricated synthetic drains, structured concrete cell, post-tensioned concrete platforms, drain-to-drain vacuum consolidation, and vacuum consolidation with a membrane (II-UNAM, 2016; Ossa et al., 2019). The test sections were instrumented profusely and monitored for more than 50 months, providing valuable information for the definite design adopted for the runways. The present work deals with the behaviour of the RE.

2.1 *Geometry and construction*

The RE was constructed to assess the behavior of the soft soil in Texcoco due to the presence of a typical pavement structure for airport runways and in the absence of any soil improvement technique or special foundation. Therefore, it serves as a reference to assess the performance of the different solutions considered.

Figures 1 and 2 show a plan view and a cross-section of the RE. It has a maximum central height of 2.10 m, which decreases with a symmetrical design cross slope of 1.14%. At its centre, the RE consists of a 1.0 m thick platform of light-weight gravel, a 0.5 m thick subbase course of compacted sandy silt, and a 0.6 m thick pavement structure.

2.2 *Field Instrumentation*

Instrumentation installed in the RE is summarized in Figure 3. Here, particular emphasis is placed on the data from the hydraulic settlement profiler and the piezometers; these measurements are later compared with the simulation results.

The hydraulic settlement profiler works by measuring the hydraulic head (with a vibrating wire transducer) within a liquid-filled tube connected to a reservoir. This instrument provides a continuous vertical displacement profile relative to the reservoir elevation. In this case, the tube was installed on the ground surface before construction, and readings were taken periodically during construction and some 49 months afterwards. In Figure 4, a total relative settlement of about 1.0 m can be observed during this period at the centre of the embankment. It is important to notice that the reservoir was located close to the ground surface, only 5 m away from the RE toe. Therefore, settlements at that location are affected due to the presence of the embankment. To compare them with the numerical model, analogous settlement profiles were obtained from the simulation by subtracting the settlement occurring at the reservoir location.

Vibrating wire piezometers were installed at different positions and depths. The evolution of the excess pore-water pressures due to the construction of the embankment as well as the subsequent dissipation due to consolidation is illustrated in Figure 5. Piezometers were placed before construction and, consequently, their initial (stabilised) condition was used thereafter as the initial pore-water pressure profile of the site. To consider these modifications in the simulation results, the steady-state condition at the corresponding elevation (considering the current ground deformations in the model) is added to the excess pore pressure. Hence, the resulting value may be compared with the raw field data.

The effects of regional subsidence can be ignored in the numerical simulation. Regarding the settlement profiler, as the profiler and the reservoir experience the same regional subsidence, the relative measurements of the profiler only reflect soil deformations due to the embankment. Concerning the piezometers, in most of their elevations, water pressures barely deviate from the hydrostatic condition and, therefore, it is reasonable to assume that ground deformations due to regional subsidence are negligible at those locations. This is not the case for the piezometer located at a depth of 38 m; this piezometer was not used.

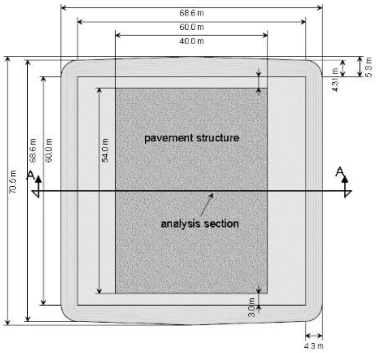

Figure 1. Plan view of the reference embankment

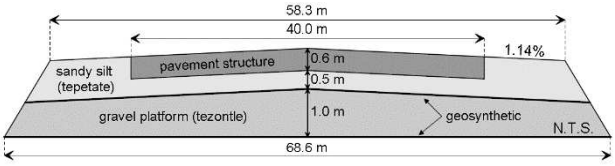

Figure 2. Cross-section of the reference embankment

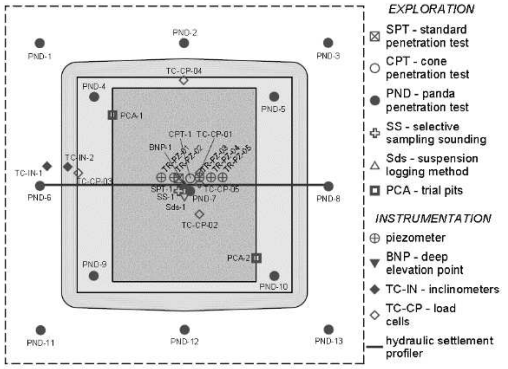

Figure 3. Exploration campaign and instrumentation at the RE site

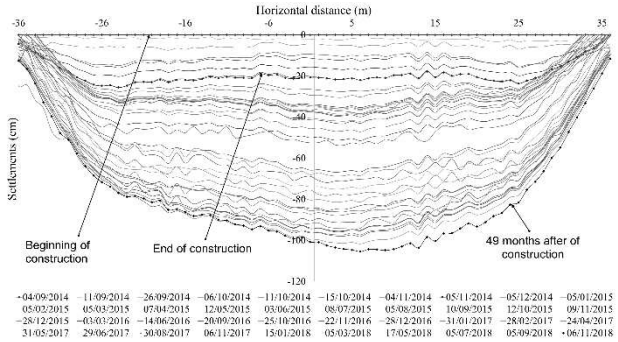

Figure 4. Settlement profiles under the reference embankment

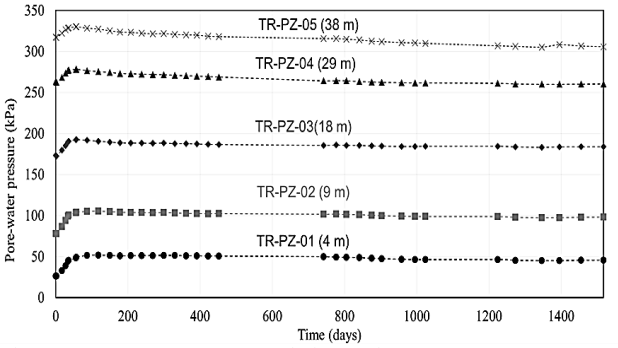

Figure 5. Pore-water pressure evolution at piezometers

3 CONSTITUTIVE MODEL

The EVP models, derived from the over-stress formulation of Perzyna (1966), are a quite successful kind of constitutive relationships to characterise the time-dependent behaviour of soils. Although the original overstress formulation of Perzyna (1966) lacked the ability to capture long-term deformations under constant loads adequately, subsequent EVP models overcame this drawback through suitable overstress functions (or viscous nuclei, or scaling functions), generally derived from laboratory observation or as extensions of available 1D formulations. Examples can be found in Adachi and Okano (1974), Adachi and Oka (1982), Katona (1984), di Prisco and Imposimato (1996), Yin and Graham (1999), Kimoto and Oka (2005). A comprehensive review can also be found in Liingaard

et al. (2004). A variation of the EVP model by Yin and Graham (1999) is adopted here to characterise the clayey soft soil deposits for the simulation and interpretation of the RE.

The MCC isotropic yield function (Roscoe and Burland, 1968) is employed in Yin and Graham (1999) to characterise the flow surface, which generally does not conform to the observed yield envelopes in soft natural clays (Graham et al.1983; Smith et al. 1992). In addition, the importance of considering anisotropy in the simulation of soft clay deposits has been highlighted before (Zdravkovic et al. 2002). A variation of the Yin and Graham (1999) model is adopted here, replacing the MCC ellipse by the anisotropic yield function of Wheeler et al. (2003) as proposed by Zhou et al. (2005). However, the rotational hardening law put forth by Wheeler et al. (2003) was also incorporated to account for the evolution of anisotropy with deformation unlike Zhou et al. (2005) where the inclination of the yield function was assumed to be constant during plastic deformation.

3.1 *EVP model (Yin and Graham, 1999)*

In the EVP model (Figure 6), total strain rates are decomposed in an elastic and a viscoplastic components, as shown Eq. (1)

$$\dot{\boldsymbol{\varepsilon}} = \dot{\boldsymbol{\varepsilon}}^{\mathrm{e}} + \dot{\boldsymbol{\varepsilon}}^{\mathrm{vp}} \tag{1}$$

Here, elastic strains are characterised by a Cam-Clay type nonlinear elasticity, where a linear behaviour is obtained in a $v - \ln p$ plot (where $v = 1 + e$ is the specific volume, $p = 1/3\,(\sigma_{xx} + \sigma_{yy} + \sigma_{zz})$ is the mean stress, and σ_{ii} are the normal components of the stress tensor $\boldsymbol{\sigma}$) with a slope equal to κ, which is a material parameter. This results in a bulk modulus given by Eq. (2)

$$K = \frac{v\,p}{\kappa} \tag{2}$$

The full elastic stiffness matrix in this case was assembled by assuming a constant Poisson's ratio ν. Viscoplastic strain rates are computed as shown in Eq. (3)

$$\dot{\boldsymbol{\varepsilon}}^{\mathrm{vp}} = S\frac{\partial f}{\partial \boldsymbol{\sigma}} \tag{3}$$

where S is the scale function and f is the flow surface. As mentioned earlier, f is characterised by the MCC yield function given by Eq. (4)

$$f = p^2 - pp_{\mathrm{m}} + \frac{q^2}{M^2} = 0 \tag{4}$$

where $q = (3/2\ \mathbf{s} : \mathbf{s})^{1/2}$ is the deviator stress invariant, $\mathbf{s} = \boldsymbol{\sigma} - \mathbf{I}p$ is the stress deviator tensor, $\mathbf{I}$ is the identity tensor, M is the slope of the critical state line in the $p - q$ plane, and p_{m} is the effective mean stress. By assuming that the stress state always lies on the flow surface, p_{m} can be determined from Eq. (5)

$$p_{\mathrm{m}} = p + \frac{q^2}{pM^2} \tag{5}$$

The latter is some sort of consistency condition in this viscoplastic formulation. Following Eq. (3), the volumetric viscoplastic strain rate is given by Eq. (6)

$$\dot{\varepsilon}_{\mathrm{v}}^{\mathrm{vp}} = S\frac{\partial f}{\partial p} = S(2p - p_{\mathrm{m}}) \tag{6}$$

Then, by equating Eq. (6) to the viscoplastic vertical strain rate from the 1D model in Yin and Graham (1994) (which is also a volumetric strain rate) the scaling function in Eq. (3), for a generalised stress space, can be obtained as shown in Eq. (7)

$$S = \frac{\psi/v}{t_{\mathrm{o}}}\exp\left[-\left(\varepsilon_{\mathrm{vm}} - \varepsilon_{\mathrm{vmo}}^{\mathrm{ep}}\right)\frac{v}{\psi}\right]\left(\frac{p_{\mathrm{m}}}{p_{\mathrm{mo}}}\right)^{\frac{\lambda}{\psi}}\frac{1}{\partial f/\partial p} \tag{7}$$

where ψ and t_{o} are two material parameters controlling the time-dependent behaviour, $\varepsilon_{\mathrm{vm}}$ is the current volumetric strain, $\varepsilon_{\mathrm{vmo}}^{\mathrm{ep}}$ and p_{mo} define the position of the reference timeline, and λ is the slope of the latter in a $v - \ln p$ plot. Details of the 1D EVP model and on the meaning of parameters are not given here and can be found in Yin and Graham (1994, 1999).

3.2 *Anisotropic flow surface (Wheeler et al., 2003)*

The SCLAY-1 model (Wheeler et al., 2003) is an anisotropic elastoplastic constitutive model for normally consolidated or slightly preconsolidated clays. The anisotropy of plastic behaviour is represented through an inclined yield surface and a rotational component of hardening to model the development of fabric anisotropy during plastic straining (Figure 7). The yield surface is given by Eq. (8)

$$f = (q - \alpha p)^2 - (M^2 - \alpha^2)(p_{\mathrm{m}} - p)p = 0 \tag{8}$$

where α defines the inclination of the major axis of the ellipse with respect to the p'axis (Figure 7), and it is a measure of the degree of plastic anisotropy of the soil. With $\alpha = 0$, the behaviour is isotropic (the MCC criterion is recovered). The rotational hardening law of Eq. (9) describes the evolution of α, due to plastic straining and is given by

$$d\alpha = \mu\left[\left(\frac{3q}{4p'} - \alpha\right)\langle d\varepsilon_p^p\rangle + \beta\left(\frac{q}{3p'} - \alpha\right)\left|d\varepsilon_q^p\right|\right] \tag{9}$$

where $d\varepsilon_p^p$ y $d\varepsilon_q^p$, are the volumetric and deviatoric plastic strain increments respectively. The parameter μ controls the absolute value of anisotropy and the parameter β is a parameter controlling the relative effect of deviator and volumetric plastic strains on the evolution of the yield function. $\langle\cdot\rangle$ are the Macaulay brackets accounting for the positive part of $d\varepsilon_p^p$. In order to extend the 1D model from Yin and Graham (1994) to the anisotropic case, in the same way as in section 3.1, but now adopting the Eq. (8) as the flow surface. The scaling function takes the same form as Eq. (7), but with $\partial f/\partial p$ derived from Eq. (8).

Equations (8) and (9) should be expressed considering the deviatoric stress tensor and the anisotropy tensor to represent the complete anisotropic version, which includes the possibility of rotation in the principal stress directions given by Wheeler et al. (2003) as shown in Eq. (10) and (11)

$$f = \tfrac{2}{3}(\{\mathbf{s} - p\boldsymbol{\alpha}_{\mathrm{d}}\} : \{\mathbf{s} - p\boldsymbol{\alpha}_{\mathrm{d}}\}) - \left(M^2 - \tfrac{3}{2}\boldsymbol{\alpha}_{\mathrm{d}} : \boldsymbol{\alpha}_{\mathrm{d}}\right)(p_{\mathrm{m}} - p)p = 0 \tag{10}$$

and

$$d\alpha_{\mathrm{d}} = \mu\left[\left(\frac{3\mathbf{s}}{4p'} - \boldsymbol{\alpha}_{\mathrm{d}}\right)\langle d\varepsilon_p^p\rangle + \beta\left(\frac{\mathbf{s}}{3p'} - \boldsymbol{\alpha}_{\mathrm{d}}\right)\left|d\varepsilon_q^p\right|\right] \tag{11}$$

where the anisotropy tensor is given by Eq. (12)

$$\boldsymbol{\alpha}_{\mathrm{d}} = \begin{bmatrix} \frac{1}{3}(2\alpha_{xx} - \alpha_{yy} - \alpha_{zz}) \\ \frac{1}{3}(-\alpha_{xx} + 2\alpha_{yy} - \alpha_{zz}) \\ \frac{1}{3}(-\alpha_{xx} - \alpha_{yy} + 2\alpha_{zz}) \\ \alpha_{yz} \\ \alpha_{xz} \\ \alpha_{xy} \end{bmatrix} = \begin{bmatrix} \alpha_{xx} - 1 \\ \alpha_{yy} - 1 \\ \alpha_{zz} - 1 \\ \alpha_{yz} \\ \alpha_{xz} \\ \alpha_{xy} \end{bmatrix} \tag{12}$$

The same approach than in Sivasithamparam et al. (2015) is adopted, where the components of the deviator fabric tensor ($\boldsymbol{\alpha}_{\mathrm{d}}$) are derived from an initial scalar value α_{o} as shown in Eq. (13), (14) and (15)

$$\alpha_{xx} = \alpha_{zz} = 1 - \frac{\alpha_{\mathrm{o}}}{3} \tag{13}$$

$$\alpha_{yy} = 1 + \frac{2\alpha_{\mathrm{o}}}{3} \tag{14}$$

$$\alpha_{yz} = \alpha_{xz} = \alpha_{xy} = 0 \tag{15}$$

In this case, $\varepsilon_{\mathrm{v}}^{\mathrm{p}}$ and $\varepsilon_{\mathrm{d}}^{\mathrm{p}}$ in Eq. (11) are substituted by $\varepsilon_{\mathrm{v}}^{\mathrm{vp}}$ and $\varepsilon_{\mathrm{d}}^{\mathrm{vp}}$, the latter being the volumetric and deviatoric invariants of the viscoplastic strain tensor $\boldsymbol{\varepsilon}^{\mathrm{vp}}$. The described EVP model was implemented as a user-defined soil model in the finite

element code Plaxis (Brinkgreve et al., 2019). A first-order forward Euler scheme, with an error controlled sub-stepping algorithm (Sloan, 1987), was adopted in the implementation.

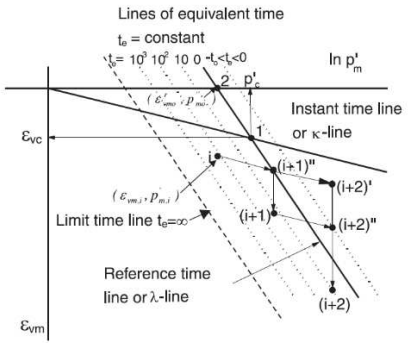

Figure 6. EVP model (Yin and Graham, 1999)

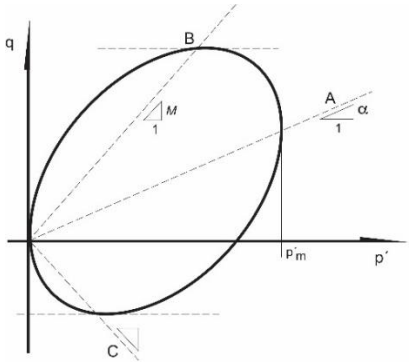

Figure 7. Anisotropic yield surface (Wheeler et al., 2003)

4 NUMERICAL SIMULATION

4.1 *Main features of the numerical model*

Interpretation of field measurements at the RE was conducted through numerical analyses using the finite element code Plaxis (Brinkgreve et al., 2019). It was assumed that the central section, where most of the instruments are located (Figure 3), can be approximated by means of 2D simulations assuming plane strain conditions. The geometry, boundary conditions, and the FE mesh employed are depicted in Figure 8. The mesh comprises 10044 triangular 15-noded finite elements with fourth-order interpolation and 12 integration points. Due to symmetry, only half of the embankment was considered.

In order to characterize the subsoil of the site, field (Figure 3) and laboratory investigation campaigns were carried out (e.g. Geotec, 2013; II-UNAM, 2015). Figure 9 shows results of the CPT-1 and SPT-1 tests and the initial pore-water pressure profile derived from piezometers TR-PZ-01 to TR-PZ-05; depletion from the hydrostatic condition is evident for depths greater than 23 m. The initial pore-water pressure profile was used thereafter as the initial pore-water pressure profile of the model. The estimated initial total and effective vertical stress profiles (Figure 9) were derived from known unit weights and horizontal stresses were estimated assuming a coefficient of earth pressure at rest K_o derived from Jaky's (1994) formula. The laboratory testing program included oedometric and triaxial tests; the results were used to characterise the clayey strata.

From the available information, the idealised stratigraphy shown in Figure 9 was derived, composed of the following layers:

- *Surface crust* (SC). Shallow clayey layer, 0.8 m thick, desiccated and fissured due to the effect of solar radiation. Fissures may content fine sand deposited by wind.
- *Upper clay formation* (UCF). Clayey layer of high plasticity, high compressibility, and low undrained shear strength, 34.0 m thick, interspersed by volcanic glass and lenses of sandy and silty alluvial soils. For the analyses later described, this layer was divided into three sub-layers due to modest variations in their properties.
- *First hard layer* (FHL). A hard layer of dense sand and silt, 1.2 m thick, with some degree of cementation.
- *Lower clay formation* (LCF). Clayey layer, 7.8 m thick, quite similar to the UCF, but with lower water contents, lower compressibilities, and higher undrained shear strengths.
- *Second hard layer* (SHL). A second hard layer of dense sand and silt, 5.4 m thick, with some degree of cementation.
- *Deep clay formation* (DCF). Clayey layer, 10.8 m thick, considerably less compressible than the UCF and LCF layers.

Clayey strata are interspersed with lenses of sandy and silty alluvial soils that can be identified in the CPT sounding (Figure 9). They enhance the dissipation of pore-water pressures and, therefore, they were considered in the simulation. Three of the most relevant lenses were directly incorporated in the numerical model (Figure 8). The first one appears at a depth of 10.3 m and, because it is rather thick, it was included as a soil layer. The other two are located 21.0 and 23.0 m deep and exhibit a smaller thickness; they were simulated using the drain tool in Plaxis. Since not all lenses could be directly included in the simulation, the permeability adopted for clayey strata is somewhat larger than the permeability from intact samples. Nevertheless, employed values are within the range reported from the results of in situ tests at the site (López-Acosta et al., 2019).

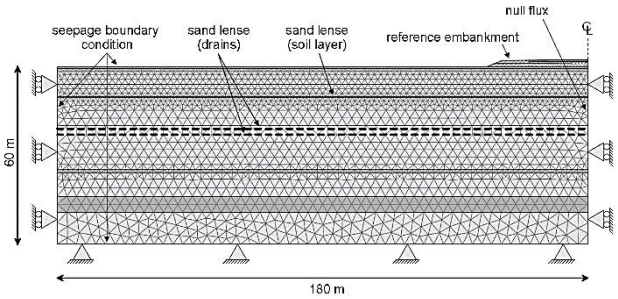

Figure 8. Geometry, boundary conditions and FE mesh employed

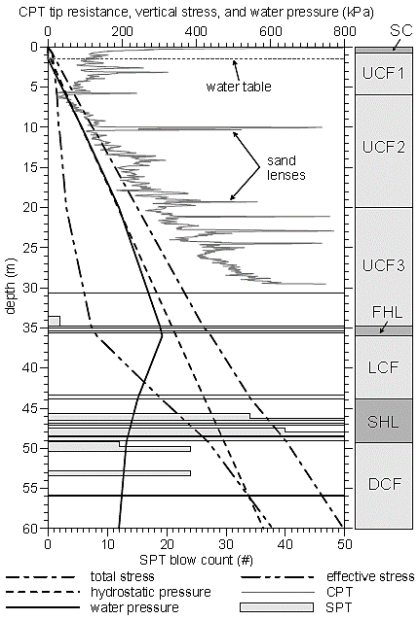

Figure 9. Subsoil conditions and idealized stratigraphy at the RE site

The surface crust, the hard layers, and the drain layer were described through an elastic perfectly plastic material, with a

Mohr-Coulomb yield envelope (Table 1). A linear elastic material was adopted for the gravel platform, the subbase course, and the pavement structure. The latter was simplified into a single cluster with weighted average properties. Finally, clayey layers were characterised with the modified EVP model described in section 3 (Tables 2a -2b). The reference time (t_0) was considered equal to 1 day for all the clayey layers. To determine the value of the viscosity parameter (ψ) the relationship C_c/C_α was considered, which according to Mesri et al. (1987) has a value of 0.35 for the Mexico City clays.

Table 1. Parameters employed for sandy/silty layers

Layer	E (kN/m^2)	c (kN/m^2)	ν (-)	ϕ (°)	K_o (-)	k (m/day)
SC	10000	20	0.25	35	0.43	9.99E-02
Lense	15000	25	0.33	35	0.43	4.80E-01
FHL	30000	30	0.33	45	0.29	9.99E-02
SHL	30000	30	0.33	45	0.29	9.99E-02

Table 2.a Parameters employed for clayey layers

Layer	Thickness (m)	e_o (-)	ν (-)	λ (-)	κ (-)	ψ (-)	OCR (-)	k (m/day)
UCF1	5.20	6.67	0.2	1.60	0.120	0.051	1.32	9.5E-4
UCF2	4.00	7.74	0.2	3.15	0.140	0.099	1.33	1.7E-4
UCF2	9.40	7.74	0.2	3.15	0.140	0.099	1.33	1.7E-4
UCF3	14.80	6.53	0.2	2.75	0.099	0.099	1.31	9.3E-4
LCF	7.80	3.42	0.3	1.03	0.052	0.048	1.40	4.0E-5
DCF	10.80	3.42	0.3	1.03	0.052	0.048	1.40	4.0E-5

Table 2.b Anisotropy parameters employed for clayey layers

Layer	Thickness (m)	Unit weight (kN/m^3)	M (-)	K_o (-)	α_o (-)	μ (-)	β (-)
UCF1	5.20	11.62	1.85	0.293	0.10	6.33	0.91
UCF2	4.00	11.90	1.55	0.384	0.45	8.37	1.01
UCF2	9.40	11.90	1.55	0.384	0.45	8.37	1.01
UCF3	14.80	12.00	1.64	0.357	0.65	8.05	1.02
LCF	7.80	13.64	1.59	0.371	0.63	13.07	1.02
DCF	10.80	13.64	1.59	0.371	0.63	13.07	1.02

The construction of the RE, was simulated by the sequential activation of the corresponding clusters. The activation of a given cluster was performed assuming undrained conditions, followed by a subsequent consolidation phase where the dissipation of excess pore water pressure is allowed. The last consolidation stage starts at the end of construction and lasted 1462 days.

4.2 *Results*

Results from the simulation were compared with field measurements. The time equal to zero corresponds to the beginning of construction. Figure 10 shows the evolution of ground settlements, at the centre of the RE, corresponding to both field measurements and simulation results. An excellent agreement can be noticed during construction. After construction, settlements from the simulation followed closely the field data after about 200 days.

Between 200 and 900 days field observations showed abnormal behaviour and abrupt changes in the settlement rate. As a result of problems with the profiler readings, the data in the highlighted area of Figure 10 was considered unreliable. These issues were eventually corrected and, since a current reading does not depend on previous ones, observations outside of the highlighted area are considered reliable. Simulation results followed a continuous trend of behaviour and captured satisfactorily the total settlement (at the centre of the embankment) at the end of the observation period.

Figure 11 depicts the settlement profiles for different construction stages, a very good correspondence can be observed. The same correspondence can be observed in Figure 12, depicting settlement profiles for 901, 1167 y 1462 days after the end of construction. Field data from both figures were constructed from the information of the settlement profiler.

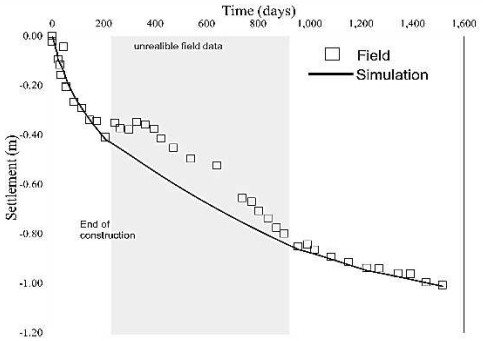

Figure 10. Evolution of ground settlements at the centre of the RE

In Figure 13, the evolution of pore-water pressures, at different depths, is compared with the simulation results. This figure illustrates how water pressures increased considerably at the clayey layers during the construction process. Ground deformations at this stage occur, to a large extend, under undrained conditions. Pressure increases due to construction were accurately reproduced in piezometers TP-PZ-02, TP-PZ-03 and TP-PZ-04. In piezometer TP-PZ-01, pressure increases were somewhat overestimated. The latter occurs most likely due to the sand lenses that were not directly included in the analysis, which enhance dissipation. Nevertheless, the overall performance of the numerical simulation to reproduce the water pressure response is satisfactory.

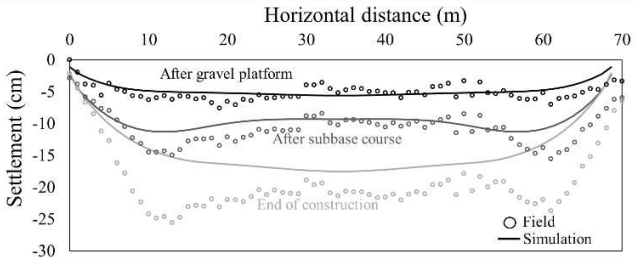

Figure 11. Settlement profiles under the RE during construction

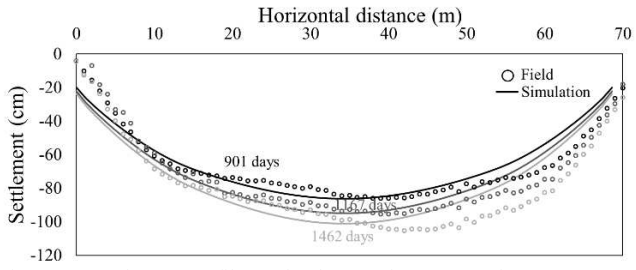

Figure 12. Settlement profiles under the RE after construction

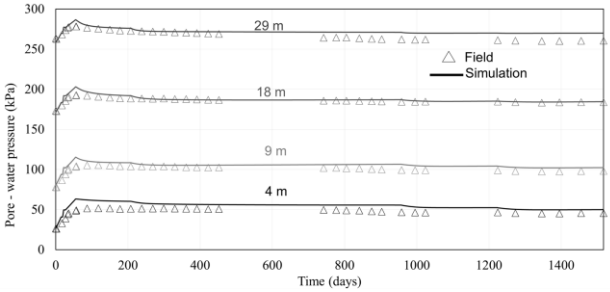

Figure 13. Pore-water pressure evolution

5 CONCLUSIONS

This paper presented a finite element analysis of the Reference embankment constructed to assist in the design of the runways for the now-cancelled NAICM project. An extension to the three-dimensional case of a well-known 1D viscoplastic model, was implemented within a commercial finite element code to simulate the behavior of clay soil strata. The constitutive model adopts an anisotropic flow surface and a rotational hardening law. The advantage offered by the implemented model is that it incorporates key characteristics of the Mexico City clay behavior such as time dependence, long-term deformations and an anisotropic flow Surface. A limitation of the model implemented is that it is applicable only to normally consolidated and slightly preconsolidated clays.

Results derived from the simulation were compared with the field observations in terms of the evolution of the surface settlements and the response of the pore-water pressure at different depths. It follows that the simulation was able to reproduce quite well the observed behavior. Therefore, the implemented model represents an appealing alternative to characterize the behavior of Mexico City clay for calculations in engineering practice. Finally, in the case study considered here, the stress increments were not close to a failure condition and it seems that the anisotropic flow surface had only a moderate influence on the results obtained. However, this may be only true for this case and this is certainly an issue that deserves further investigation.

6 REFERENCES

Adachi, T., y Oka, F. (1982). "Constitutive equations for normally consolidated clay based on elasto-viscoplasticity." *Soils and Foundations,* 22(4), 57–70.

Adachi, T., y Okano, M. (1974). "A constitutive equation for normally consolidated clay." *Chemical Pharmaceutical Bulletin,* 14(4), 55–73.

Brinkgreve, R. B. J., Kumarswamy, S., Swolfs, W. M., Zampich, L., y Ragi-Manoj, N. (2019). *"PLAXIS 2019 user manual."* Plaxis bv, Delft, Netherlands.

Di Prisco, C., y Imposimato, S. (1996). "Time dependent mechanical behaviour of loose sands." *Mechanics of Cohesive-Frictional Materials,* 1(1), 45–73.

Geotec. (2013). Estudios de exploración del subsuelo y pruebas de laboratorio en el terreno, para atender la demanda de servicios aeroportuarios en el centro del país. 123-O12-DTCN013S, Ciudad de México.

Graham, J., Noonan, M. L., y Lew, K. V. (1983). "Yield states and stress-strain relationships in a natural plastic clay." *Canadian Geotechnical Journal,* 20(3), 502–516.

II-UNAM. (2015). Evaluación en Geotecnia y Estructuras para Resolver la Problemática del Transporte Aéreo en el Centro del País. *Convenio de Colaboración No. ASA-UNAM-13-002,* Ciudad de México.

II-UNAM. (2016). Investigaciones y estudios especiales relacionados con aspectos geotécnicos del Nuevo Aeropuerto Internacional de la Ciudad de México (NAICM) en el vaso del exlago de Texcoco, Zona Federal. *Convenio de Colaboración No. GACM/DCI/SJ/CI/013-2015,* Ciudad de México.

Jaky, J. (1944). "The coefficient of earthpressure at rest. In Hungarian (A nyugalmi nymas tenyezoje)." *Journal of the Society of Hungarian Engineers and Architects,* 355–358.

Katona, M. G. (1984). "Evaluation of viscoplastic cap model." *Journal of Geotechnical Engineering,* 110(8), 1106–1125.

Kimoto, S., y Oka, F. (2005). "An elasto-viscoplastic model for clay considering destructuralization and consolidation analysis of unstable behavior." *Soils and Foundations,* 45(2), 29–42.

Liingaard, M., Augustesen, A., y Lade, P. V. (2004). "Characterization of models for time-dependent behavior of soils." *International Journal of Geomechanics,* 4(3), 157–177.

Lopez-Acosta, N. P., Espinosa-Santiago, A. L., y Barba-Galdámez, D. F. (2019). "Characterization of soil permeability in the former Lake Texcoco, Mexico." *Open Geosciences,* 11(1), 113–124.

Mesri, G., y Castro, A. (1987). "Cα/Cc concept and K0 during secondary compression." *Journal of Geotechnical Engineering,* 113(3), 230–247.

Mitchell, J. K. (1956). "The fabric of natural clays and its relation to engineering properties." *35th Annual meeting of the Highway Research Board,* Washington, D.C., 693–713.

Mooser, F. (1956). "Los ciclos de vulcanismo que formaron la Cuenca de México." *XX Congreso geológico internacional,* Ciudad de México.

Ossa, A., Botero, E., Madrigal, M. C., Ovando, E., Mendoza, M., y López-Acosta, N. P. (2019). "Performance of a pavement foundation system based on the partial compensation of masses method." *Soils and Foundations,* 59(2), 351–366.

Ovando-Shelley, E. (2011). "Some geotechnical properties to characterize Mexico City Clay." *Pan Am CGS Geotechnical conference,* Toronto.

Ovando-Shelley, E., Ossa, A., y Romo, M. P. (2007). "The sinking of Mexico City: Its effects on soil properties and seismic response." *Soil Dynamics and Earthquake Engineering,* 27(4), 333–343.

Ovando-Shelley, E., Ossa, A., y Santoyo, E. (2013). "Effects of regional subsidence and earthquakes on architectural monuments in Mexico City." *Boletín de la sociedad geológica mexicana,* 65(1), 157–167.

Perzyna, P. (1966). "Fundamental problems in viscoplasticity." *Advances in Applied Mechanics*, 9, 243–377.

Roscoe, K. H., y Burland, J. B. (1968). "On the generalized stress-strain behavior of 'wet' clay." *Engineering Plasticity, J. Heyman and F. A. Leckie, eds., Cambridge University Press, Cambridge,* 535–609.

SCT. (2014). "Declaratoria de saturación en el campo aéreo del Aeropuerto Internacional de la Ciudad de México Benito Juárez." *Diario Oficial de la Federación, Ciudad de México*.

Sivasithamparam, N., Karstunen & Bonnier P.G. (2015). "Modelling creep behavior of anisotropic soft soil". *Computers and Geotechnics,* 69 (2015) 46-57.

Sloan, S. W. (1987). "Substepping schemes for the numerical integration of elastoplastic stress–strain relations." *International Journal for Numerical Methods in Engineering,* 24(5), 893–911.

Smith, P. R., Jardine, R. J., y Hight, D. W. (1992). "The yielding of Bothkennar clay." *Géotechnique,* 42(2), 257–274.

Valderrama, Y. V. (2013). "Investigación experimental del comportamiento de las arcillas bajo pequeñas deformaciones." *Universidad Nacional Autónoma de México.*

Vázquez-Sánchez, E., y Jaimes-Palomera, R. (1989). "Geología de la Cuenca de México." *geofísica Internacional,* 28(2), 133–190.

Wheeler, S. J., Näätänen, A., Karstunen, M., y Lojander, M. (2003). "An anisotropic elastoplastic model for soft clays." *Canadian Geotechnical Journal,* 40(2), 403–418.

Yin, J.-H., y Graham, J. (1994). "Equivalent times and one-dimensional elastic viscoplastic modelling of time-dependent stress-strain behaviour of clays." *Canadian Geotechnical Journal,* 31, 42–52.

Yin, J.-H., y Graham, J. (1999). "Elastic viscoplastic modelling of the time-dependent stress-strain behaviour of soils." *Canadian Geotechnical Journal,* 36(4), 736–745.

Zdravković, L., Potts, D. M., y Hight, D. W. (2002). "The effect of strength anisotropy on the behaviour of embankments on soft ground." *Géotechnique,* 52(6), 447–457.

Zentar, R., Karstunen, M., Wiltafsky, C., Schweiger, H. F., y Koskinen, M. (2002). "Comparison of two approaches for modelling anisotropy of soft clays." *Proc. 8th international symposium on numerical models in geomechanics* (NUMOG VIII), G. N. Pande and S. Pietruszczak, eds., A.A. Balkema, Rome, 115–121.

Zhou, C., Yin, J.-H., Zhu, J.-G., and Cheng, C.-M. (2005). "Elastic anisotropic viscoplastic modeling of the strain-rate-dependent stress– strain behavior of K0-consolidated natural marine clays in triaxial shear tests." Int. J. Geomech., 5(3), 218–232.